

## Crosswell electromagnetic tomography: System design considerations and field results

M. J. Wilt\*, D. L. Alumbaugh†, H. F. Morrison\*\*, A. Becker\*\*, K. H. Lee§,  
and M. Deszcz-Pan‡‡

### ABSTRACT

Electrical conductivity is an important petroleum reservoir parameter because of its sensitivity to porosity, pore fluid type, and saturation. Although induction logs are widely used to obtain the conductivity near boreholes, the poor resolution offered by surface-based electrical and electromagnetic (EM) field systems has thus far limited obtaining this information in the region between boreholes. Low-frequency crosswell EM offers the promise of providing subsurface conductivity information at a much higher resolution than was previously possible. Researchers at Lawrence Livermore National Lab (LLNL) and Lawrence Berkeley Laboratories (LBL), together with an industrial consortium, recently began a program to conduct low-frequency crosswell EM surveys and develop suitable inversion techniques for interpreting the data.

In developing the field instrumentation we used off-the-shelf components whenever possible, but cus-

tom-designed induction coil transmitters and receivers were built for the field experiments. The assembled field system has adequate power for moderate to high-resolution imaging, using boreholes spaced up to 500 m apart. The initial field experiment was undertaken in flat lying terrain at the British Petroleum test site in Devine, Texas. Using wells spaced 100 m apart, we collected a complete crosswell EM data set encompassing a 30 m thick, 10 ohm-m limestone layer at a depth of 600 m. The resulting profiles were repeatable to within 1% and showed an excellent sensitivity to the layered structure, closely matching the borehole induction resistivity log. At the UC Richmond field station, crosswell EM measurements were made to track an injected slug of salt water. Conductivity images of data collected before and after injection showed a clear anomaly as a result of the salt water plume and indicated that the plume had migrated in a northerly direction from the injection borehole.

### INTRODUCTION

An important problem in petroleum production is the development of a reservoir model that guides the drilling of wells and the management of the field. Ideally the model provides a 3-D numerical representation of the petroleum-bearing rock, properties of the reservoir units, and the nature of the boundaries. To construct this model the reservoir engineer has only the detailed data from well logs in a limited number of holes, a geologic conceptual model, and structural controls provided by seismic data. The ex-

trapolation of drill hole data to the interwell volume is an area where geophysics can be of great benefit. Using high-resolution geophysics to assign physical properties to the model is a relatively new and exciting idea which could revolutionize the effectiveness of reservoir simulation. Papers by Lake (1990), Shelton and Cross (1989), and Savit (1987) eloquently state the need for this.

Seismic velocity and electrical conductivity are affected by the porosity, saturation, temperature, and anisotropy of typical reservoir rocks, and consequently seismic and electrical techniques are a first choice in the search for new

Manuscript received by the Editor September 20, 1993; revised manuscript received October 11, 1994.

\*Lawrence Livermore National Lab, P.O. Box 808, L-156, Livermore, CA 94550.

†Formerly Lawrence Berkeley Laboratory; presently with Sandia National Laboratory, P.O. Box 5800, MS 0750, Albuquerque, NM 87185-0750.

\*\*Dept. of Mineral Engineering, 577 Evans Hall, University of California at Berkeley, Berkeley, CA 94720.

§Lawrence Berkeley Laboratory, 1 Cyclotron Rd., Berkeley, CA 94720.

‡‡Formerly Lawrence Berkeley Laboratory; presently with U.S. Geological Survey, Box 25046, MS 964, Denver Federal Center, Denver, CO 80225.

© 1995 Society of Exploration Geophysicists. All rights reserved.

reservoir characterization methods. Surface-based 3-D seismic methods have already had a large impact on reservoir engineering by providing detailed maps of the geometry of producing formations and in some cases hydrocarbon distribution (Sherriff, 1992). This is a significant departure from their traditional role of finding target structure in an exploration program.

Electrical conductivity has a more direct relationship to reservoir fluid properties than do seismic parameters because porosity, pore fluid conductivity, saturation, and temperature all influence the conductivity. Even though electrical logs are indispensable to the reservoir engineer for assessing saturation, pore fluid type, and indirectly, permeability, electrical logging measures the conductivity in the vicinity of the borehole to a radius of only a few meters. Means are now at hand to map the conductivity on a reservoir scale and it is this prospect that motivates this study of cross-borehole electromagnetic methods.

Although seismic methods are relatively mature, the methodology for measuring electrical conductivity on a reservoir scale is in a developmental stage. Surface low-frequency electromagnetic and dc resistivity methods have been applied to process monitoring (Wayland et al., 1984; Bartel and Wayland, 1981; Bartel and Ranganayaki, 1990), but they have been limited to identifying the presence and general configuration of relatively shallow processes. High-frequency EM (greater than 1 MHz) has been used in crosswell configurations since the early eighties (Kretzschmar et al., 1982; Laine, 1987), but in most sedimentary formations the low resistivity limits the propagation distance of these fields to a few meters (Harben and Pihlman, 1988).

Crosshole and borehole-to-surface configurations typically offer improved sensitivity as compared to surface-based schemes. In surface surveys, the fields must first penetrate to the target zone, produce a secondary or scattering current, and the fields from these currents then attenuate greatly in returning to the surface. This attenuation obviously limits the sensitivity of small features at depth. A further complication in surface methods is that the near-surface weathered layer is invariably inhomogeneous and thus exerts a strong attenuation and distortion of the fields from deep targets. Getting at least one of the transmitter-receiver pair near the target zone alleviates these problems somewhat (Greaves et al., 1991; Asch and Morrison, 1989) but an even greater improvement occurs if both the source and receiver are placed in boreholes. For example, crosshole dc resistivity surveys have far greater resolution than surface or surface-to-borehole configurations (Daily and Owen, 1991; Shima, 1990).

The work of Zhou (1989) initiated a systematic study of low-frequency crosswell EM for reservoir scale problems and showed that a low-frequency analog of seismic diffraction tomography provided good resolution of interwell features. With the aid of an industrial consortium, researchers at LLNL, LBL, and the University of California, Berkeley began a joint program to conduct low-frequency crosswell and surface-to-borehole EM surveys and to develop suitable inversion and imaging codes for interpreting field data. The objective of the program was to develop tools for reservoir characterization and process monitoring.

Theoretical and numerical model development for this method are discussed in a companion paper in this issue (Alumbaugh and Morrison, this issue). In this paper we describe survey design, the equipment that we used for crosswell measurements, and give results from two field surveys.

#### DESIGN OF A CROSSWELL EM SYSTEM

In this section we describe the criteria for designing a crosswell EM system, making use of simple models to determine the optimum transmitter power (dipole moment), receiver sensitivity, and the operating frequencies. Other design considerations include allowable dimensions (i.e., to deploy in boreholes), weight, and durability.

Spies and Habashy (1992) show that for the zeroth order Born approximation the 'sensitivity of a given source receiver pair to the region between the wells is given by the Frechet derivative,

$$K_{Hz} = \sigma_b G^{hz} E_{\phi b}, \quad (1)$$

where  $\sigma_b$  is the background conductivity,  $E_{\phi b}$  is the tangential electric field, and  $G^{hz}$  is the magnetic field Greens function.

Figure 1 shows the amplitude of  $K_{Hz}$ , assuming a cylindrical geometry for a point centered between a source and receiver at the same depth. The kernel is plotted as a function of the background induction number ( $\sigma_b \omega \mu R^2$ ) to determine the sensitivity for a range of frequency-conductivity-interwell spacings. The scattered field for an electrically small body is proportional to this sensitivity function. The abscissa of this graph starts at an induction number of 0.01 and terminates at 1000. Below 0.01 the total field is almost equal to that of the free space value (Spies, 1992), above 1000 the fields are difficult to measure because of attenuation.

Several important characteristics about crosswell EM can be derived from this diagram. At induction numbers less

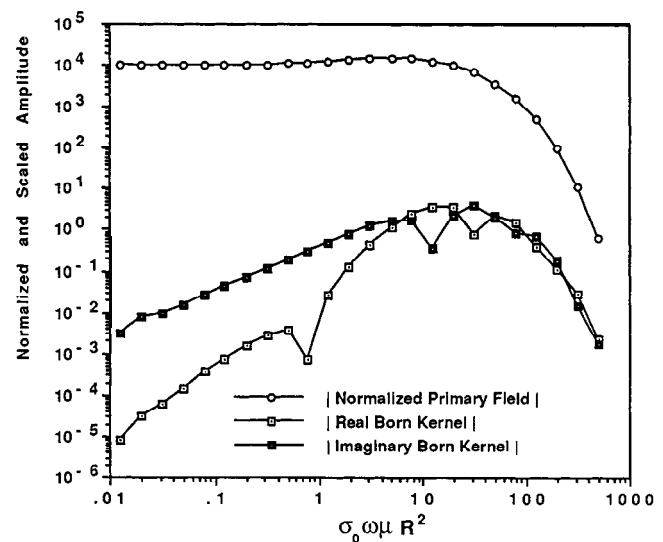


FIG. 1. Plot of the Frechet derivative for coplanar magnetic dipoles.

than 1.0 the scattered field is small, indicating that the response of small or poor conductors will be difficult to measure. The kernel amplitude is maximum at induction numbers from five to 100. This corresponds to two to 10 plane-wave skin depths, where the skin depth is defined as the distance a plane wave attenuates to  $1/e$  its initial value and is given by  $\delta = \sqrt{2/\sigma\omega\mu}$ . In this region the scattered fields will be most easily detected; we can therefore use it as a rule of thumb when designing surveys. For induction numbers above 100 both the kernel and the primary field fall off rapidly because of attenuation.

We can obtain a minimum value of transmitter moment required by noting that for coplanar vertical magnetic dipole transmitters and receivers in a conductive whole space the magnetic field is given by:

$$H_z = \frac{-M}{4\pi r^3} e^{-ik_b r} (1 + ik_b r - k_b^2 r^2) \quad (2)$$

(Jackson, 1962, p 398). Here,  $M$  is the transmitter dipole moment,  $r$  is the inter-well distance, and  $k_b$  is the propagation constant of the background medium as defined by

$$k_b^2 = \omega^2 \mu \epsilon - j\sigma_b \omega \mu. \quad (3)$$

Neglecting the first term of equation (3), which at audio frequencies in earth materials is many times smaller than the second term, the vertical magnetic field in this geometry is a function of conductivity-frequency product and separation only. In Figure 2 we plot the vertical magnetic field amplitude for coplanar transmitter-receiver pairs. The plot gives the field for a range of well separations, frequencies, and conductivities using a transmitter moment of 1; it also shows the "noise floor," assuming that the noise is equal to the maximum sensitivity of our existing receiver, or  $10^{-7}$  nT. Note that by increasing the transmitter moment the noise floor moves downward proportionately. For example, using a transmitter moment of  $10^3$  A-m<sup>2</sup> moves the noise floor from  $10^{-7}$  to  $10^{-10}$  nT. Note that up to an abscissa of  $\sigma f r^2 = 4 \times 10^6$  the plots in Figure 2 display the  $1/r^3$  fall-off characteristic of dipolar EM fields in free space; above this the attenuation is exponential.

Figure 2 is also useful for designing field surveys. Assuming a background conductivity of 0.1 S/m and a source moment of  $10^3$  A-m<sup>2</sup>, the figure shows that we can do effective crosswell imaging at tool separations from 10 to more than 1000 m. At a well separation of 100 m and a background conductivity of 0.1 S/m, the plot indicates that frequencies in the range from 100-100,000 Hz can be used for imaging.

#### LLNL/LBL CROSSWELL EM SYSTEM

Using the above design criteria, we assembled and tested crosswell EM systems for two field trials. For the deep test in Devine, Texas, we used wells 100 m apart and several km deep. For the shallow test at Richmond, California, we used wells less than 50 m apart and 100 m deep. In practice the two field systems were identical except for the transmitter tool and associated winch.

The measurement system is modular. The transmitter section includes a borehole solenoid, a current source to

power the solenoid, and a winch and cable system for downhole deployment. The receiver module consists of a commercial sensor attached to a winch and cable system and a commercial synchronous detector which uses the optically coupled transmitter current signal as a reference. Data are recorded using a desktop computer.

Transmitter and receiver modules for this system are essentially separate entities. That is, the receiver may be used with separate transmitters, and separate receivers may be operated using the same transmitter. The modules are connected via electrically isolated cables. Instrumentation from each module is required to be locally grounded, to have its own power supply, and to be electrically isolated from other modules. Such grounding and isolation is vital for the elimination of stray currents and ground loops that degrade data quality.

#### Transmitter Section

A schematic diagram of our crosswell transmitter system is given in Figure 3. Although a downhole oscillator is preferred, for simplicity the initial transmitter was powered from the surface. We built our first transmitter around a laminated magnetic steel (mu-metal) core previously used on an airborne EM system (the McPhar F-400). This core was chosen because of its availability and the relatively low frequency (100-4,000 Hz) required for the Devine test. It is 2.4 m long and 7.5 cm in diameter, and when wound uniformly with 350 turns of wire, this solenoid has an effective relative magnetic permeability of about 150 and an inductance of about 40 mH. A moment of 1000 A-m<sup>2</sup> is achieved with a current of 5 A.

The maximum moment is limited by the current and the number of turns required to saturate the core with magnetic field. This, in turn, is determined by the volume and type of core material. For this particular mu-metal core the maximum moment is approximately 10 000 A-m<sup>2</sup>. The associated inductive reactance is canceled by series tuning the solenoid with an appropriate capacitor located in the solenoid casing. Core losses rise very sharply with frequency as a result of hysteresis effects and eddy currents induced in the conductive steel core. About 1 kW of power is required to drive the solenoid with 5 A when the frequency is raised to 1 kHz. Above 5 kHz the output is reduced to unacceptable levels.

Because of the higher projected operating frequency and closer well spacing at the Richmond test site, we built a transmitter solenoid with a ferrite core. Ferrite is preferred at high frequencies because it is essentially nonconductive and therefore not susceptible to eddy current losses. We constructed a tubular core made up of a large number of stacked ferrite toroids. The resulting tube has an outside diameter of 4.4 cm, an inner diameter of 1.91 cm, and a length of 197 cm. Although a solid ferrite core of the same dimension has almost twice the magnetic permeability, we elected to use the toroids because they were lower in cost and readily available. The core was wound with 125 turns to maximize the output at 18 kHz. It has an inductance of about 2 mH and an effective magnetic permeability of 150. Using a current of 3.5 A we obtain a moment of about 100 A-m<sup>2</sup>.

Because of the different power requirements at the two test sites, the transmitter solenoids were driven by different

current sources in each case. At the Devine site we used a Zonge GGT-20 transmitter driver. Although this device generates a square waveform, it is filtered by the resonant transmitter circuit so that the resultant transmitted signal closely resembles a sine wave at the fundamental frequency. At the Richmond test site the power requirements could be met easily by using an ordinary laboratory signal generator coupled to a Crown model 600 power amplifier with a maximum output of 600 W.

The large transmitter coil and cable are moved with a hydraulic, diesel-powered winch; the cable drum can hold about 1500 m of seven conductor logging cable. We use a lightweight portable electrical winch that holds 200 m of cable to move the smaller ferrite coil. This lightweight winch and coil may be moved easily by two people and is convenient to use in shallow applications. For each tool the transmitter depth and rate of movement are monitored with a wheel-driven encoder/counter. In addition to providing depth information, this encoder pulse also serves as a data acquisition trigger at the receiver.

The transmitter current is detected with an inductive current monitor connected to the source output. This analog record of the current is sent to the receiver via an isolated line where it is used as a phase reference and a monitor of the transmitter flux. Note that the current is only roughly proportional to the transmitter flux because of the nonlinearity of the core material. We therefore rely on calibration corrections to determine the flux from the current measurement. A second isolated line provides an analog record of the encoder pulse.

#### Receiver Section

Signals are detected at the receiver using a vertical-axis custom-designed borehole coil (Electromagnetic Instruments Inc., model number BF8DH). This receiver coil is an ultrasensitive device [maximum sensitivity of  $10^{-13}$  teslas (T)] which operates in the frequency range from 1-100,000 Hz. The tool is housed in a pressure vessel designed for depths up to 2 km. Detected signals are amplified within the coil and then transmitted to the surface via the logging cable. At the surface they are further amplified and filtered before input to the receiver van (Figure 4). In the van, all instruments are controlled from a desktop computer via the GPIB interface. The computer can adjust instrument gains and sensitivities as well as select sample and averaging rates for the logging system.

Note that while the tool sensitivity is rated at  $10^{-13}$  T, the maximum sensitivity we have achieved is approximately  $10^{-11}$  T. This disparity is likely a result of incomplete source-receiver isolation and the effects of external noise.

Data logging at the receiver is triggered by encoder pulses originating at the transmitter. The computer counts the incoming pulses until one corresponding to a pre-selected measurement depth is received. The computer then collects transmitter current data from the digital voltmeter and magnetic field data from the lock-in detector. The lock-in detector uses the transmitter current waveform as a reference signal and detects receiver signals in-phase and out-of-phase. It is a very effective device for accurately discriminating low level signals in a noisy background.

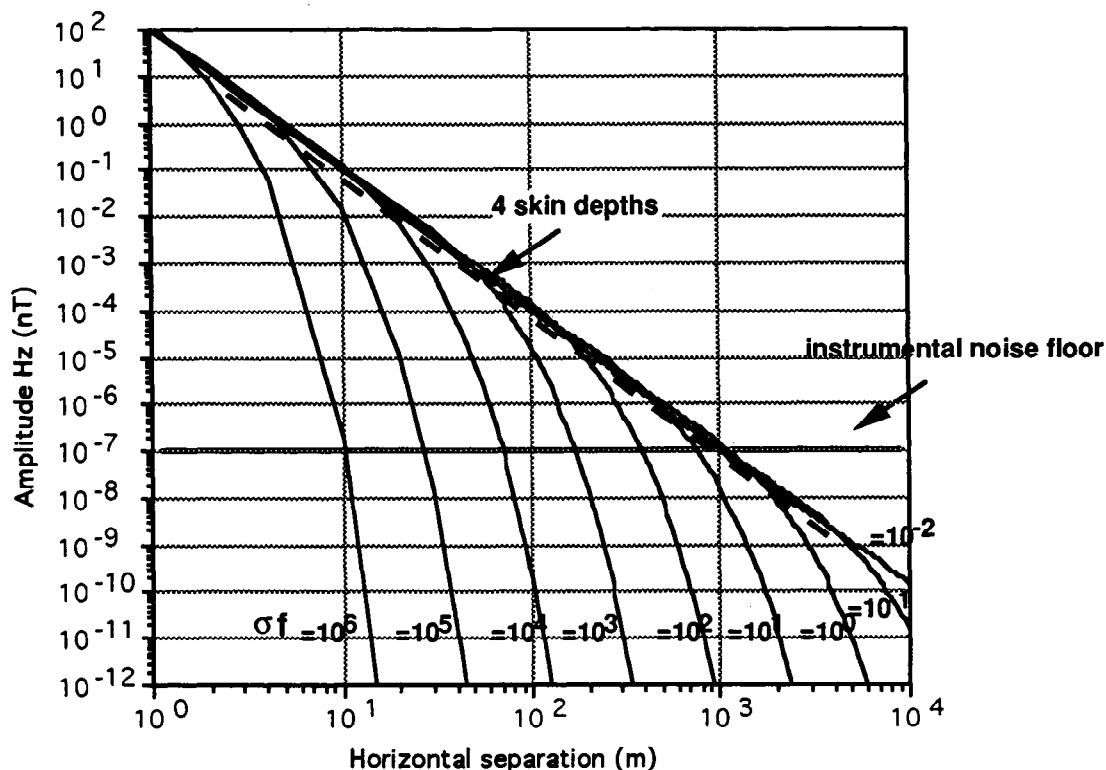


FIG. 2. Vertical magnetic field amplitude for coplanar magnetic dipoles in a wholespace. Plots are for a range of frequency-conductivity products using a source moment of 1.

## Crosswell Logging

Each borehole segment is logged by moving the transmitter coil upwards at a fixed rate while the receiver remains stationary in a separate borehole. Although equivalent information could be collected by moving the receiver coil while the transmitter is fixed, doing so results in noisy data as a result of the motion of the sensitive detector in the earth's magnetic field. The source coil is typically moved at a rate of 3-5 m/minute. This allows sufficient time for signal averaging but is still a reasonable rate for data collection.

Data are collected in  $\frac{1}{2}$ -m to 1-m intervals; at each measurement point five readings are averaged as the transmitter moves past. We typically log over a depth interval that is 1.5-2.0 times longer than the separation between boreholes; this is a minimum interval required for tomographic reconstruction (Zhou, 1989). Ten to 15 receiver stations are usually spaced to cover the depth interval traversed by the transmitter.

## FIELD TEST 1: BRITISH PETROLEUM TEST SITE DEVINE, TEXAS

The Devine test site, established by British Petroleum to test geophysical methods and instrumentation, is located some 50 km southwest of San Antonio, Texas (Figure 5). It is situated in an isolated area, away from sources of cultural

noise, but is reasonably accessible to population centers. Three boreholes are available for experimental use. Boreholes #2 and #4 are 100 m apart and are steel-cased to 160 m and plastic lined below this level to a depth of 900 m. Borehole #9 is steel-cased to a total depth of 900 m. The geology at the site consists of a sequence of sandstones, shales, and limestones. Individual beds are continuous and flat lying across the entire site as is evident from an examination of the well logs. The borehole resistivity logs show variations from 1 to 300 ohm-m with the higher resistivity layers (limestones) concentrated toward the base of the section and the sandstone and shale layers ranging in resistivity from 1 to 10 ohm-m.

We chose to collect a set of crosswell profiles that span a section from 550-670 m. This segment includes 2-3 ohm-m sands and shales and 30-m thick, 3-10 ohm-m predominantly limestone strata (see Figure 6). For each profile the source moves over a depth interval of 120 m and the receiver remains fixed in the other borehole at a level within this same depth interval. Subsequent profiles are then made between the same source positions using different receiver depths. A complete set of profiles corresponds to 13 receiver positions, spaced 8 m apart, covering a similar depth span as the source coil.

Sample crosswell magnetic field plots are given in Figure 7. The plots show the amplitude and phase of the

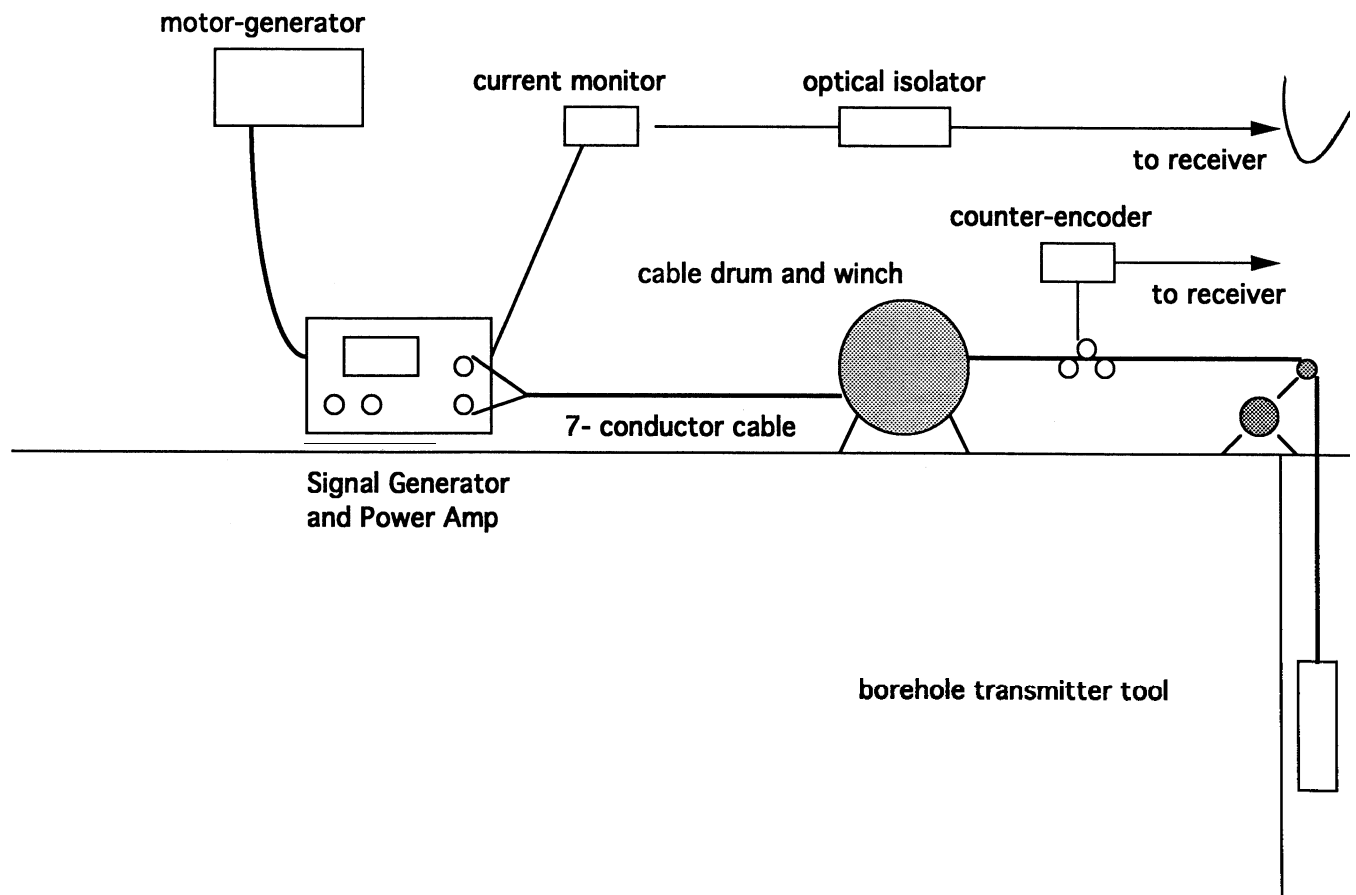


FIG. 3. Schematic diagram of the crosswell EM transmitter.

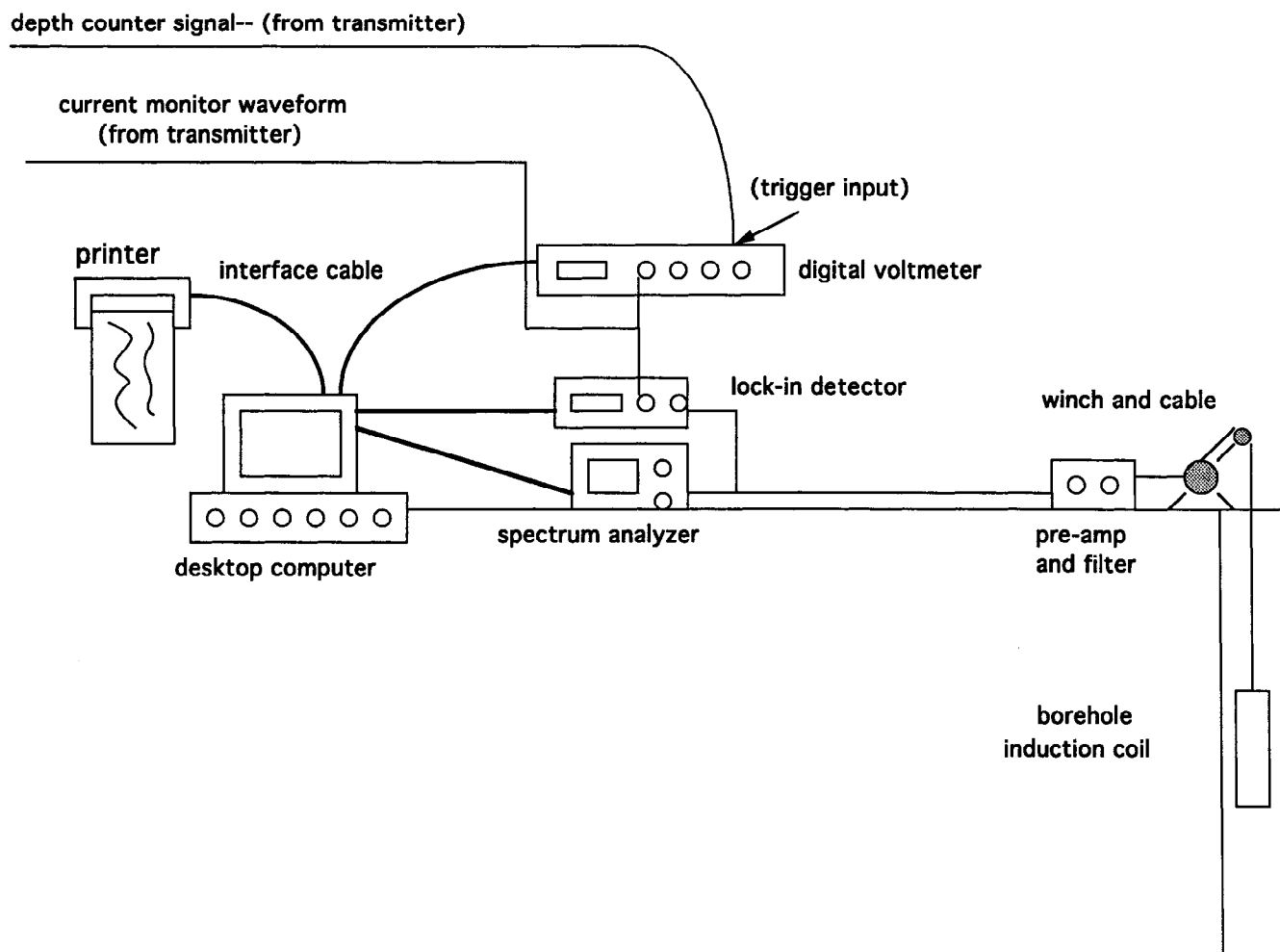


FIG. 4. Schematic diagram of the crosswell EM receiver system.

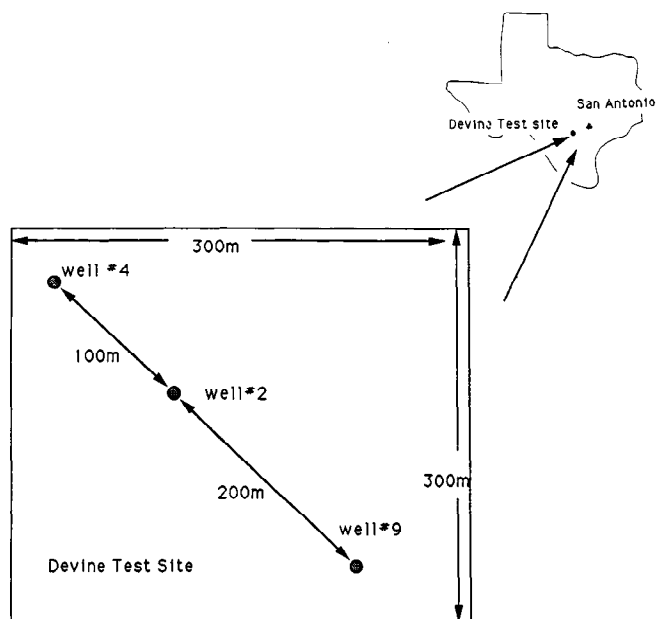


FIG. 5. Location map for the Devine, Texas, experimental facility.

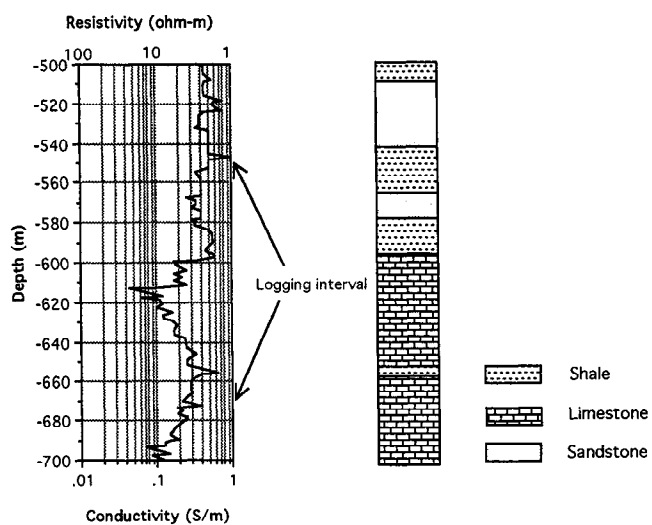


FIG. 6. Geologic section and borehole induction log for the Devine test.

vertical magnetic field at a frequency of 512 Hz as the transmitter moves between 550 m and 670 m in one borehole while the receiver is fixed at a depth of 598 m in a second borehole 100 m away. The magnetic field amplitude, given in nanoteslas (nT) per unit dipole moment, is a smooth curve that forms a peak where the source and receiver coils are in closest proximity and an approximately symmetrical decrease in field strength away from the peak. The transmitter moment is approximately  $1000 \text{ A}\cdot\text{m}^2$  so the detected fields are in tens of nT. The phase data are also smooth, but they display more inflection than the amplitudes. Near a depth of 600 m the phase forms a peak and it "rolls off" sharply above this: This sharp phase rotation correlates with a decrease in subsurface resistivity as the transmitter passes from resistive limestone below 600 m to less resistive sands and shales above this depth.

The above profile was measured twice on successive days to establish the precision of the system; the difference

between the data sets is displayed in Figure 8. This figure shows the amplitude difference over the 24-hour period to be less than 1.0% for all points with an average of 0.3%. The phase difference averaged less than  $0.2^\circ$ . Both of these are well within the guidelines of 1.0% for amplitude variations and  $0.5^\circ$  for phase established for imaging requirements (Zhou, 1989). A further quality check was the reciprocity test, made by interchanging the source and receiver coils. This test is useful in identifying systematic errors that are not evident in repeated measurements. The reciprocal measurements also agree to within 1%, but the differences are about twice as high as the repeated data shown above.

In Figure 9 we present contour plots of the 512 Hz amplitude and phase data collected at Devine. The figures consist of a collection of the data from the individual profiles plotted at the source and receiver points. The amplitude data dominantly reflect the relative positions of the source and receiver coils, peaking where the coils are in closest proximity. The peak amplitudes are larger in the deeper parts of

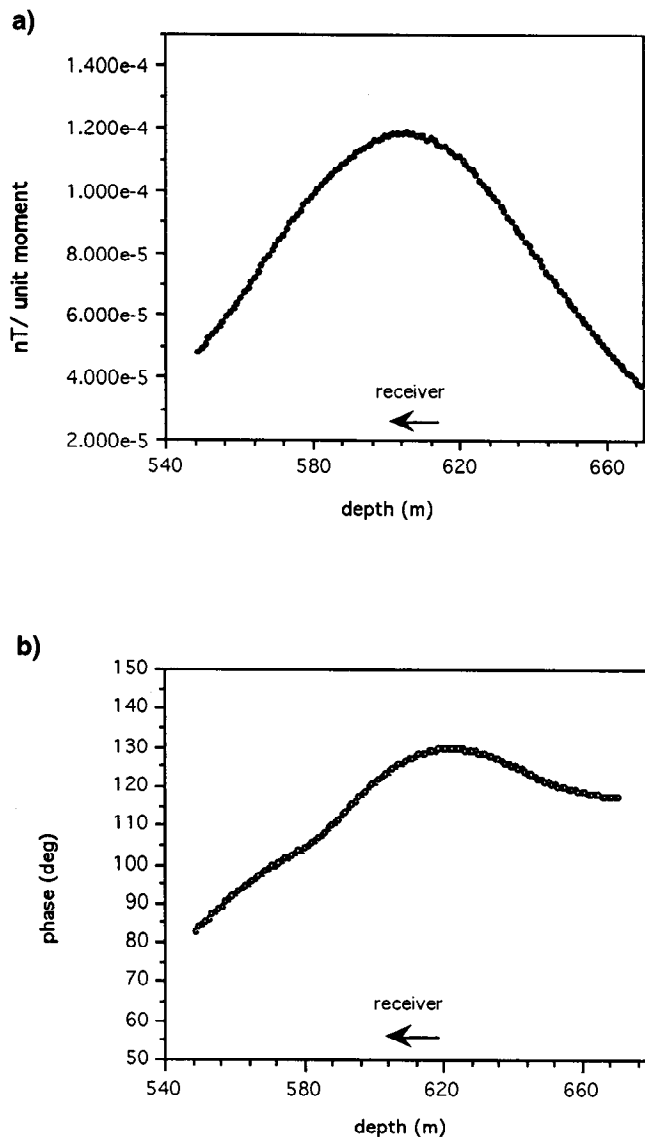


FIG. 7. Sample cross-borehole amplitude (a) and phase (b) plots.

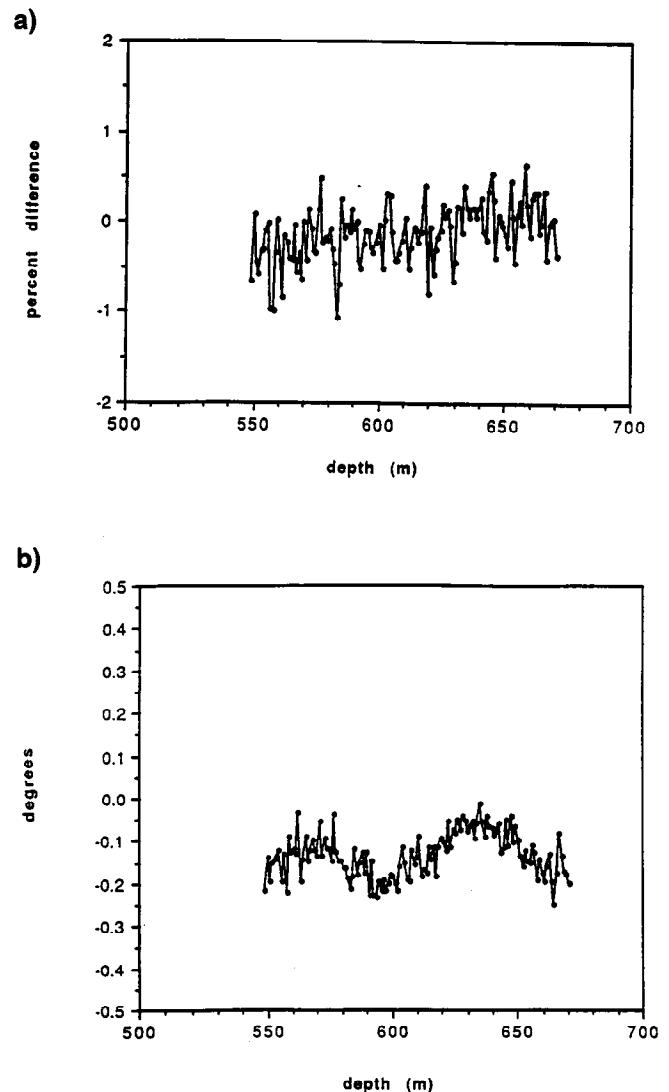


FIG. 8. Percent difference of amplitude (a) and phase difference (in degrees) (b) for a 24-hour repeat test.

the section which corresponds to a zone of higher resistivity. The phase data show a smooth, continuous variation of more than 60° within the depth span. The maximum phase values generally correspond to the high resistivity limestone; the minimum phases correspond to the lower resistivity sands and shales. The contact between these layers, located at a depth of 600 m, can be correlated with sharp gradients in the phase.

We initially interpreted the Devine data using a layered model inversion. The code is a generalized Marquardt least-squares inversion allowing surface and/or borehole magnetic or electric dipole sources and receivers. It was assembled from a forward solution (EM1D) written by Ki Ha Lee and an inversion (INSOL) subroutine described in Anderson (1982). In general, the inversions at Devine were well behaved, and layered models derived from inverting individual profiles closely agree. This is in large part a result of the simple stratified geology at the Devine site. In Figure 10 we show a comparison of the layered model inversion for the profile from receiver station 609.75 to the borehole induction log spanning the same depth interval. The resistivity values

from the inverted section and from the induction log are quite close.

Figure 11a shows a conductivity image derived from the 512 Hz Devine data using the iterative Born inversion described in Alumbaugh and Morrison (this issue). It is plotted with a smoothed version of the well log shown in Figure 6. The image indicates primarily 1-D geometry with a resistive zone, corresponding to the limestone layer, extending from approximately 600 m to 630 m in depth. The correlation between the well log and the tomogram is remarkably good, especially near the receiver well. A closer examination of the image reveals some 2-D structure which is inconsistent with the known geology at Devine. The resistive layer is shown to be thicker near the receiver well and regions above and below this are more conductive near the source well.

To determine if these 2-D artifacts are a function of the inversion algorithm or the data, we calculated a synthetic data set for a layered model using the same source-receiver geometries. The inversion of these calculated results (Figure 11b) show similar 2-D artifacts, although not as extreme. This synthetic model suggests that some of the artifacts are a result of small amounts of systematic drift in the Devine data. Alumbaugh (1993) has shown that the imaging scheme is extremely sensitive to this type of correlated noise. The artifacts can also partially be explained by a lack of vertical aperture in the survey. To demonstrate this effect, a model was calculated which extended the array 40 m upward from 550 m to 510 m. As Figure 11c indicates, the added vertical coverage improves the horizontal resolution. All layers, except the resistive zone at 560 m, now extend continuously between the wells.

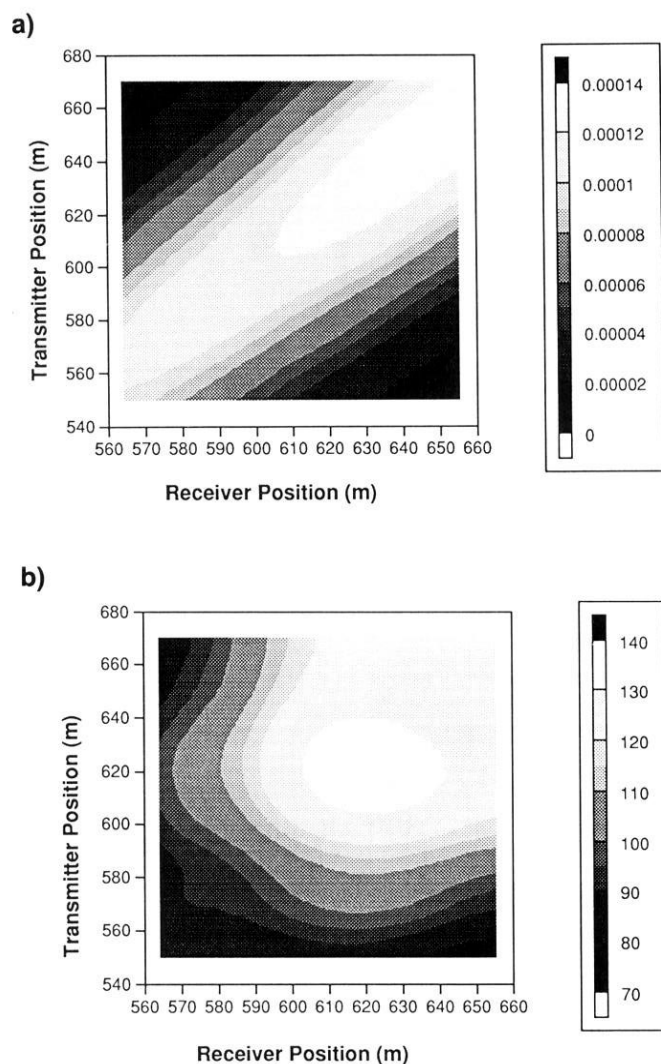


FIG. 9. Contoured cross-borehole amplitude (a) and phase (b) data for the Devine survey.

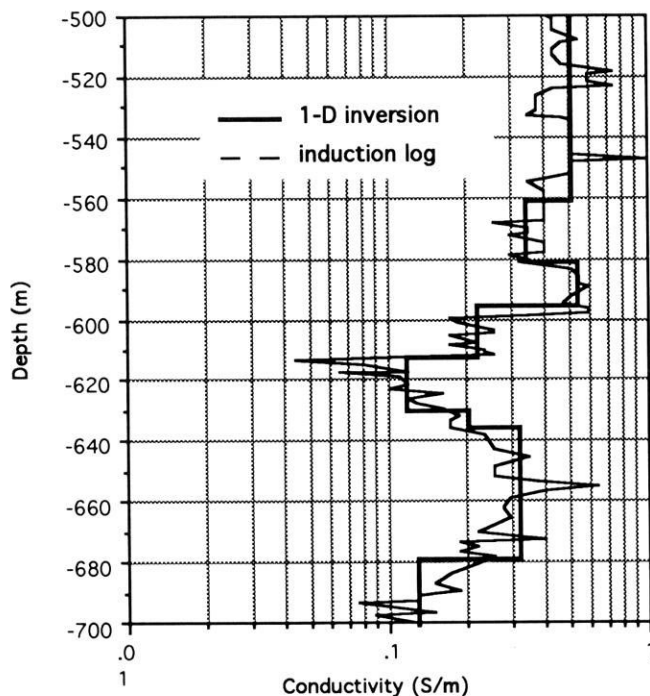


FIG. 10. Comparison of the interpreted EM results and the borehole induction log in the same interval.



Another indicator of data or model bias is the plot of the data/model misfit or residual errors. Alumbaugh and Morrison (this issue) illustrate the validity of the cylindrical assumption can be determined by examining the residual errors as a function of source and receiver depth. If this distribution exhibits a random nature, then the cylindrical geometry is valid at least to a first order. However, if the error distribution exhibits a nonrandom component, then the medium is probably more complex. In Figure 12 we plot the residual errors for the Devine inversion normalized by the maximum amplitude. The figure shows that the observed data are fit within the estimated 1% error and the error distribution exhibits a mostly random nature. This indicates that the cylindrical geometry fits the Devine geology adequately.

#### FIELD TEST 2: SALTWATER INJECTION MONITORING AT UC RICHMOND FIELD STATION

The Richmond test facility lies approximately 12 km north of the UC Berkeley campus and adjacent to the San Francisco Bay (Figure 13). From April to August, 1992 we used this facility to inject a slug of salt water and monitor its

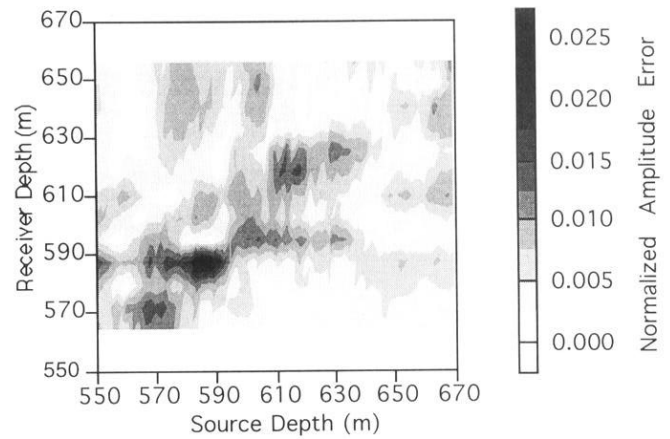


FIG. 12. Plot of the data/model misfit residual errors for the Devine inversion shown in Fig. 11a.

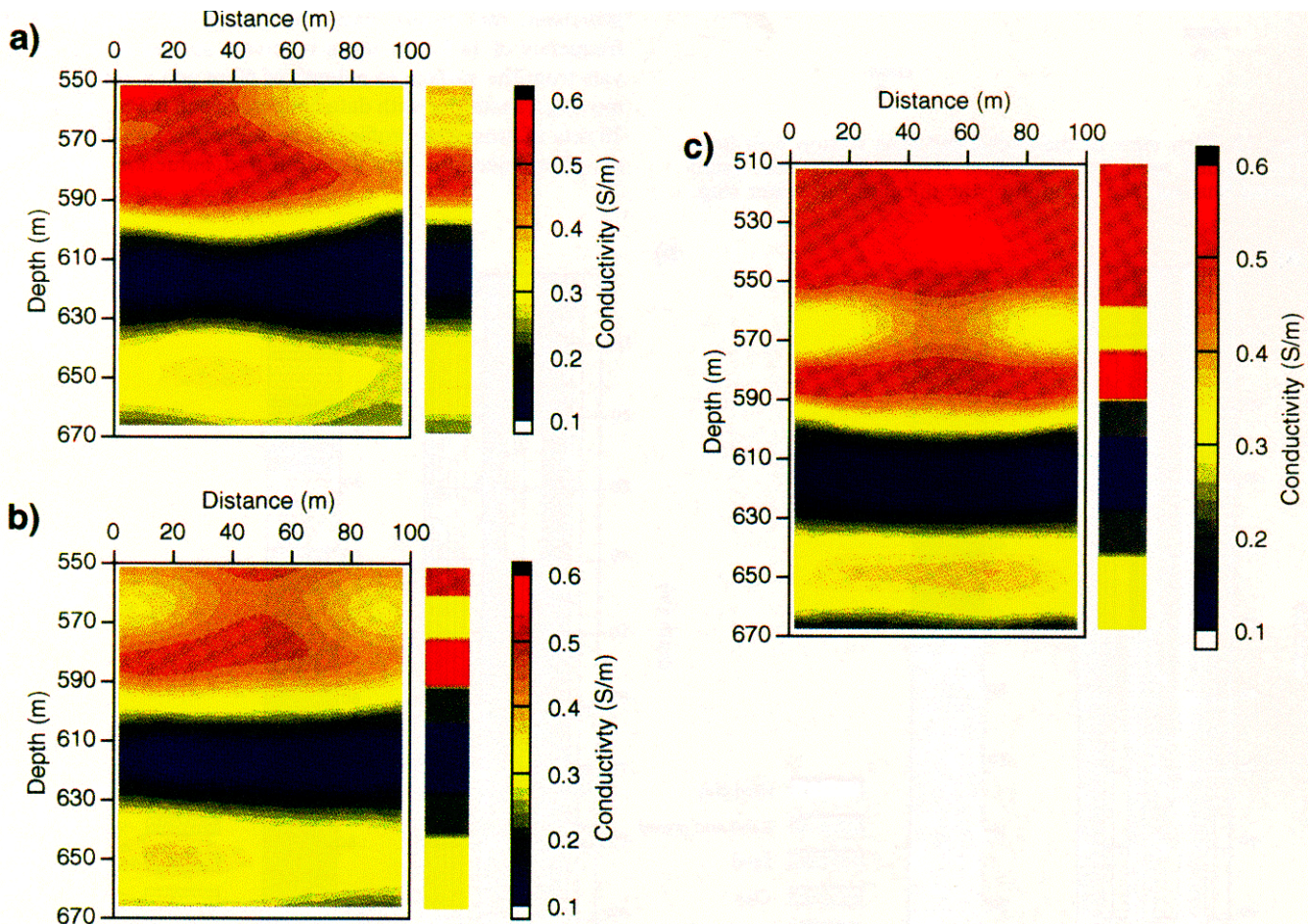


FIG. 11. Iterative Born image of the Devine crosswell EM results (a), Iterative Born inversion using computer-generated data from a forward model (b). Iterative Born inversion for vertically extended section using computer-generated data from a forward model (c).

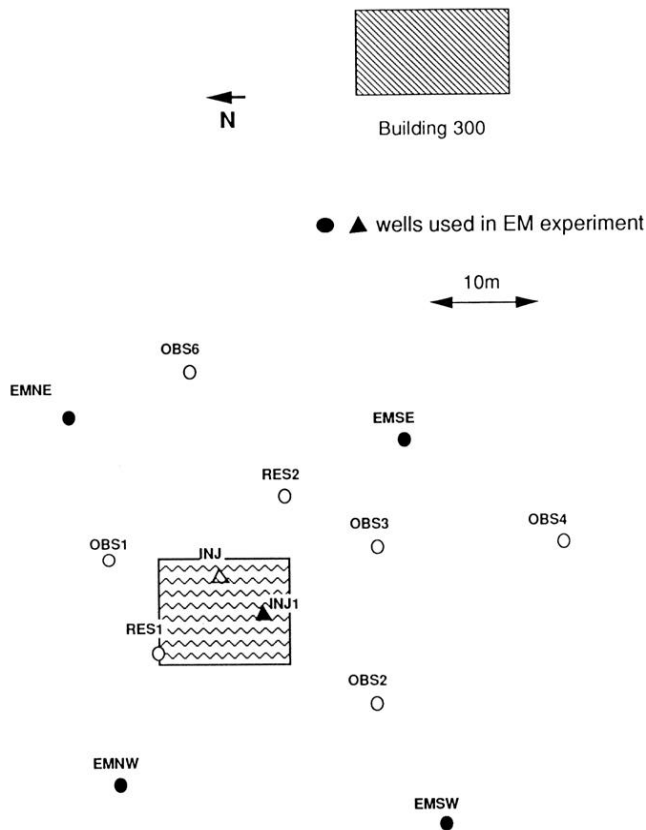


FIG. 13. Plan view of the Richmond field station well field. The shaded area near borehole INJ1 indicates the interpreted final surface location of the injected salt water slug.

emplacement and movement with crosswell EM. For the experiment we injected 250 000 liters of 1 ohm-m saltwater into a 4-m thick aquifer at a depth of 26 to 30 m through a perforated zone in well INJ1. EM were collected data before and after injection.

Figure 14 shows borehole induction logs from wells EMSW and EMNE together with stratigraphic logs made from well cuttings. The upper 30-35 m at Richmond field station consists of discontinuous unconsolidated muds, silts, and variably thick layers of sand and gravel with resistivities ranging from 5 to 30 ohm-m. Below the unconsolidated sediments is a basement consisting of sandstone or shale, most likely from the Cenozoic Great Valley formation. The sandstone basement encountered beneath boreholes INJ, INJ1, EMSE, EMSW, and EMNW has a resistivity of 100 ohm-m or more; the shale found beneath EMNE has a resistivity of 40-60 ohm-m. A description of the site geology is provided in Pouch (1987).

The crosswell EM measurements were made using a five-well set with the transmitter deployed in the central borehole (INJ1) while placing the receiver tools in the other boreholes (EMNE, EMNW, EMSE, and EMSW). This arrangement provides the first-order cylindrical symmetry required by our present imaging code (Alumbaugh and Morrison, this issue). The EM data were collected at a frequency of 18.5 kHz using receivers spaced at 5 m intervals from the surface to a depth of 60 m and a continuously moving transmitter with data collected each 0.5 m. A total of 10 sets of crosswell profiles were collected, four before and six after injection. We also collected induction resistivity

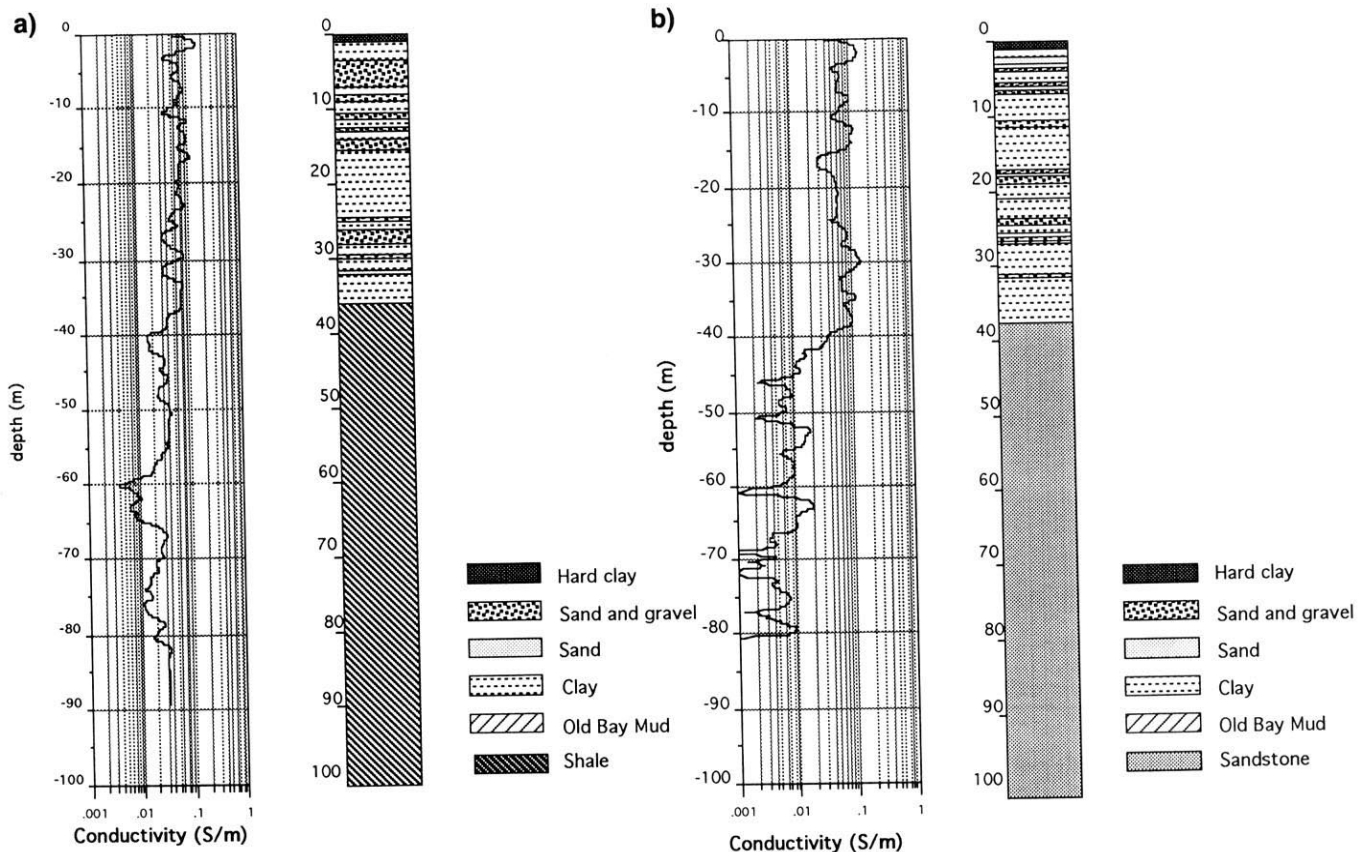


FIG. 14. Borehole induction logs from well EMNE (a) and EMSW (b) at UC Richmond field station.

logs and measured water conductivity in all holes before and after salt water injection.

To ensure that the system was operating properly, transmitter profiles were repeated at the beginning of each day and whenever the receiver was moved to a new well. In general an average of 2% amplitude error and  $1^\circ$  phase difference were considered good repeatability bounds for the system.

Extra sets of post-injection data were collected in the EMNW and EMSW wells five days and two weeks after the original data, respectively, for error and noise analysis. The overall mean error between the original and repeat measurements are 2.2% amplitude and  $0.8^\circ$  phase for EMNW and 3.3% amplitude and  $1.1^\circ$  phase for EMSW. The larger errors in EMSW may be due in part to the greater distances between INJ1 and EMSW and to the larger times between repeats.

In Figure 15 we show two induction logs from borehole INJ1, the injection well, collected before and after salt water injection. From a depth of 23 to 31 m, the logs are a mirror image because the higher resistivity sands and gravels before the injection have become the lower resistivity units after the salt water injection. The largest decrease is observed in a 4-m thick sandy-gravel aquifer at a depth of 26 to 30 m where the well is perforated. The sediments in this interval have decreased in resistivity from 15 ohm-m to 3.5 ohm-m. Using a dirty sand model (Waxman and Thomas, 1974), we predicted that the salt water should change the formation resistivity to 3 ohm-m. For these calculations we assume a

porosity of 25%, clay content of 20%, and salt water conductivity of 1 S/m.

Crosswell EM amplitude and phase measurements made before and after salt water injection appear to be only subtly different; the effects of the injection become apparent if we calculate the secondary fields resulting from the introduction of the plume. This is a simple process involving the subtraction of the fields measured before and after injection.

We show the resulting anomalies for wells EMNW and EMSW in Figures 16 and 17. Figure 16 indicates large changes centered around the injection depth, whereas the secondary fields in EMSW appear noisier and show a smaller and markedly different anomaly in the injection zone. Secondary fields in EMNE and EMSE are intermediate between the cases shown above. This suggests that the salt water plume is located asymmetrically about well INJ1 and may be moving to the north.

We interpreted the crosswell EM data at Richmond by inverting the pre- and post-injection profiles for each well separately. This was necessary because the irregular geology and resistive basement meant that we could not restrict our image to the injection zone. Thus, rather than inverting only for conductivity changes resulting from the injection, the entire conductivity structure between the two wells was imaged both before and after injection. The background

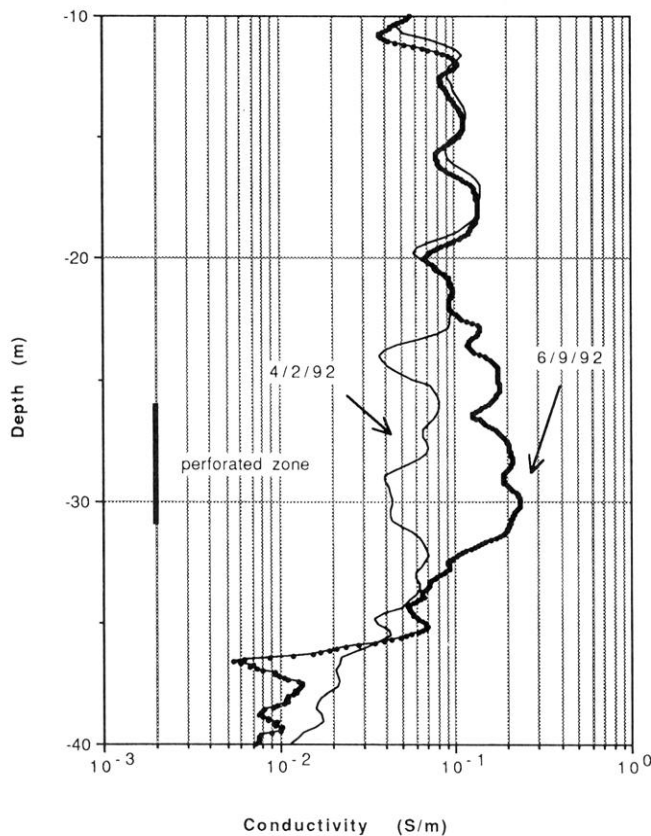


FIG. 15. Borehole induction logs in well INJ1 before and after salt water injection.

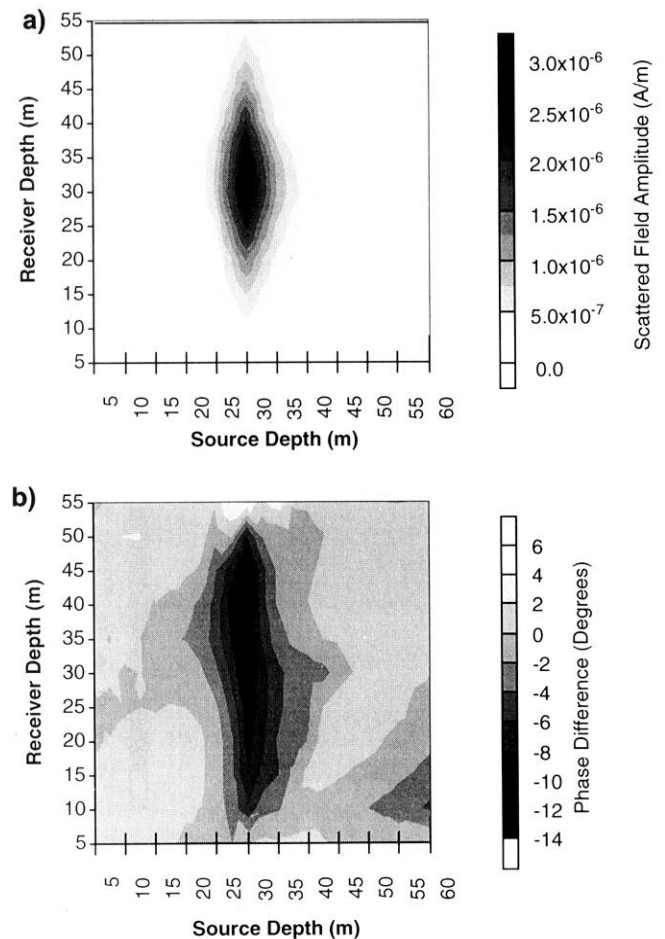


FIG. 16. Secondary field differences from borehole EMNW before and after salt water injection.



conductivity used in the inversion was chosen by minimizing the magnitude of the secondary field.

Conductivity images for EMNW before and after injection are plotted in Figures 18a and b. The pre-injection image shown in Figure 18a shows a conductive overburden overlying a more resistive basement. This is consistent with the borehole induction logs. The post injection image (Figure 18b) shows a region of high conductivity at 30 m depth near the injection well that is not present prior to injection. This anomaly corresponds to the permeable sand intersected at the injection zone and suggests that salt water has migrated within this sand to the northwest. Images of the EMNE data indicate some migration to the northeast while the EMSW and EMSE results indicate almost no migration to the southeast or southwest. This interpretation is consistent with an earlier salt water injection monitoring experiment at Richmond using the dc resistivity method (Bevc and Morrison, 1991).

The direction of plume migration becomes clear if we plot the change in conductivity before and after injection. This is a simple process of subtracting the conductivities in the pre-injection image from those in the post-injection image on

a cell by cell basis. Figure 19 shows a large conductivity increase between INJ1 and both of the northern wells. The magnitude of the change is slightly greater in EMNW than EMNE, suggesting that the salt water is moving preferentially to the northwest. To the south, the changes are much smaller in magnitude and indicate a conductivity decrease. This implies that little of the injected water is migrating southward.

A careful inspection of the images in Figures 18 and 19 shows structures that are not consistent with the known geology. Figure 18a indicates that the interface between the conductive sediments and the basement is dipping to the northwest. Although the Richmond geology is fairly complex, the well logs plotted on each side of the images show that the contact is flat. Other inconsistencies appear in the difference images (Figure 19). The conductivity changes in the EMNW and EMNE images indicate that the injection causes the sediments near the receiver wells and just beyond the plume boundaries to become more resistive. To the south, difference images indicate resistive anomalies near the injection zone and conductive anomalies near the receiver wells.

Alumbaugh and Morrison (this issue) have determined that these artifacts are a result of the cylindrical symmetry employed in the iterative Born imaging scheme. For background induction numbers above 10, a given source and receiver pair is primarily sensitive to the region immediately between them. At induction numbers below this, the array senses large areas outside of the interwell region and thus the fields generated by a given source-receiver pair contain 3-D effects which are not accounted for by the 2-D cylindrical symmetry. Because the Richmond data incorporate an induction number of approximately 4, the artifacts present in these images are probably the result of the 3-D nature of the subsurface conductivity distribution.

The residual errors between the observed and calculated data are plotted as a function of source and receiver depth in Figure 20. The error distribution does not exhibit a random nature like that observed in the Devine example (Figure 13), but the largest errors are located along the diagonal, where both the source and receiver are at similar depths. This illustrates that the artifacts present in these images are most likely products of a 3-D geology. In addition, the pre-injection and post-injection imaging errors show that a substantial error occurs at a source depth of 30 m; i.e., when the source is within the plume. Alumbaugh (1993) has demonstrated that this is likely the result of asymmetry in the plume about the source well.

To verify the direction of plume migration we employed a thin sheet model (program SHEET) originally developed by Weidelt (1981) and later modified by Zhou (1989). This model is useful for simulating some of the general characteristics observed in the data, but there are several important differences. First, we assume that the plume can be represented by an infinitesimally thin, rectangular sheet of uniform conductivity. It is known from the borehole logs, however, that the plume is at least 3-m thick and probably has an irregular 3-D shape and a nonuniform conductivity. A second major difference is that the forward modeling code restricts us to a uniform half-space for the background model; for this case we used a conductivity of 0.05 S/m.

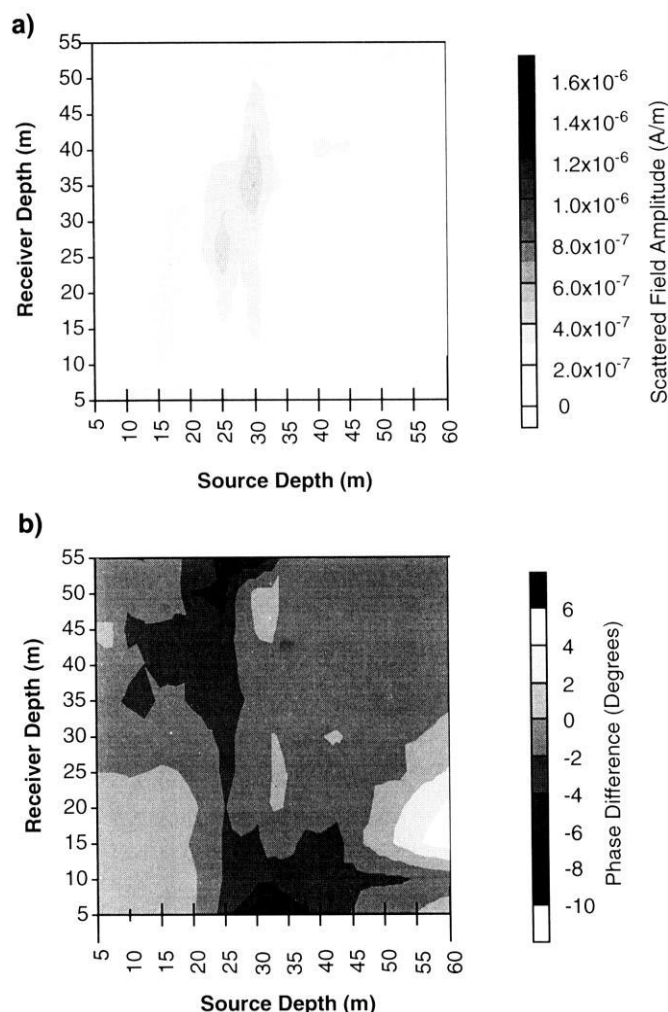


FIG. 17. Secondary field differences from borehole EMSW before and after salt water injection.

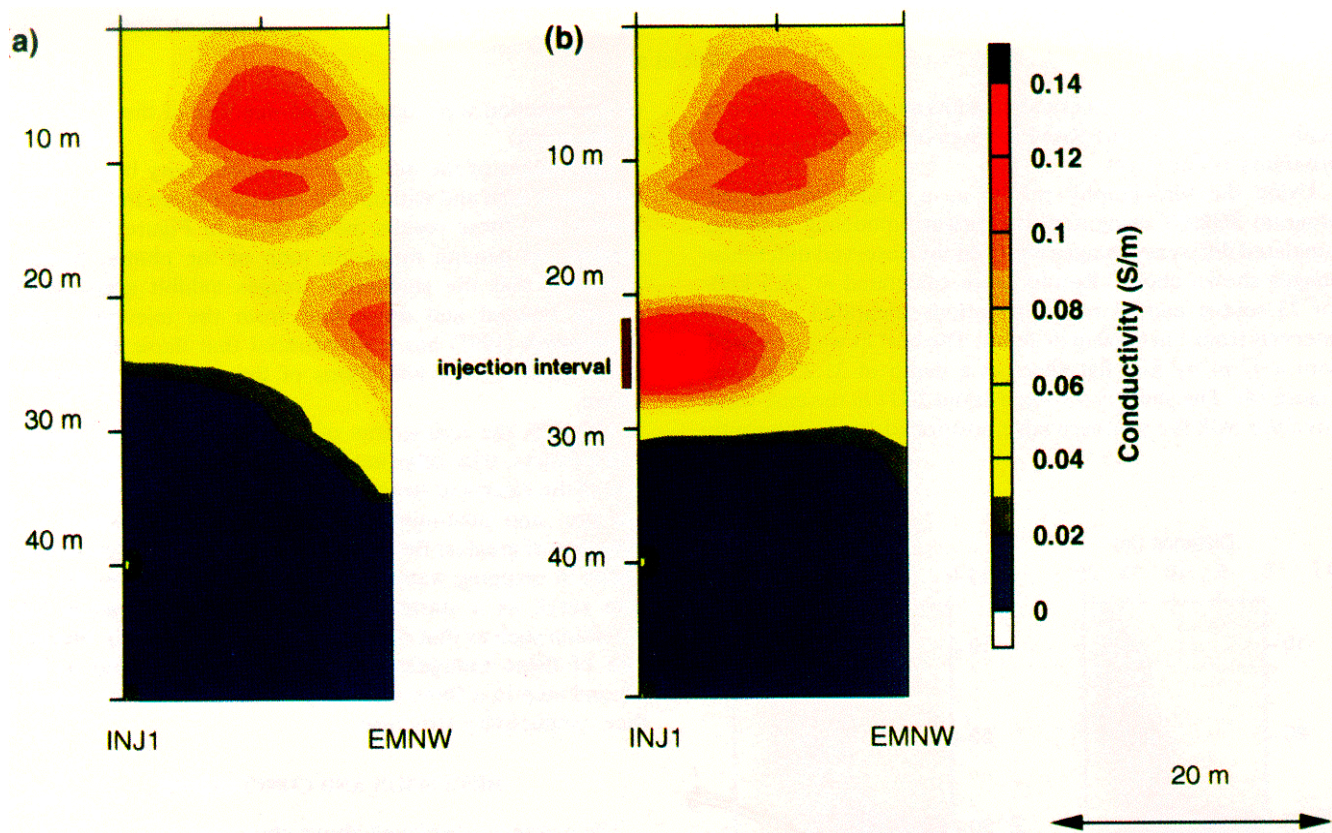


FIG. 18. Tomographic inversion of EM profile INJ1-EMNW before injection of salt water (a) and after salt water injection (b).

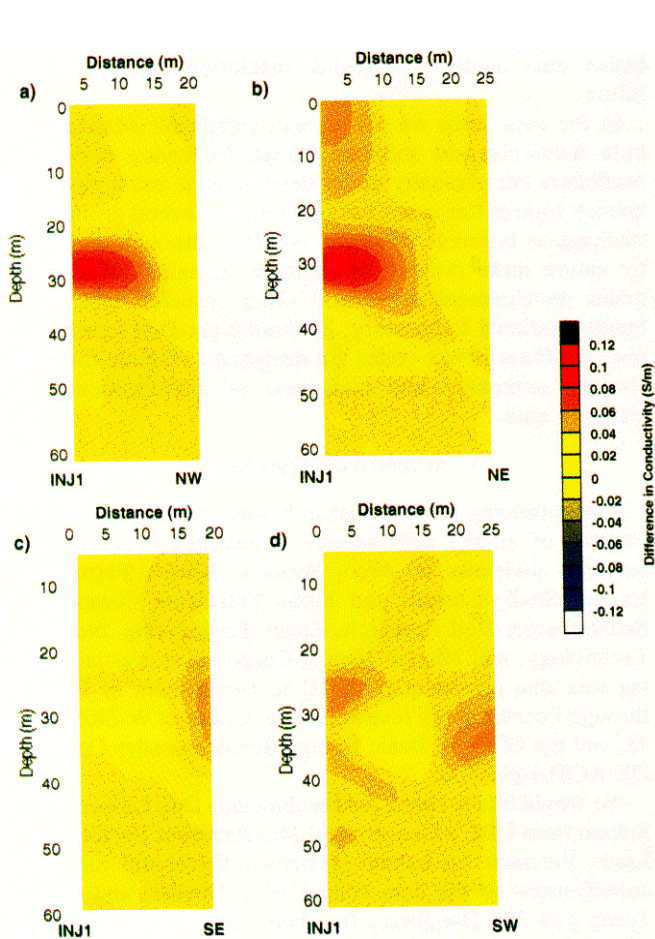


FIG. 19. Difference images of the salt water plume before and after injection for wells INJ1-EMNW (a), INJ1-EMNE (b), INJ1-EMSW (c), and INJ1-EMSE (d).

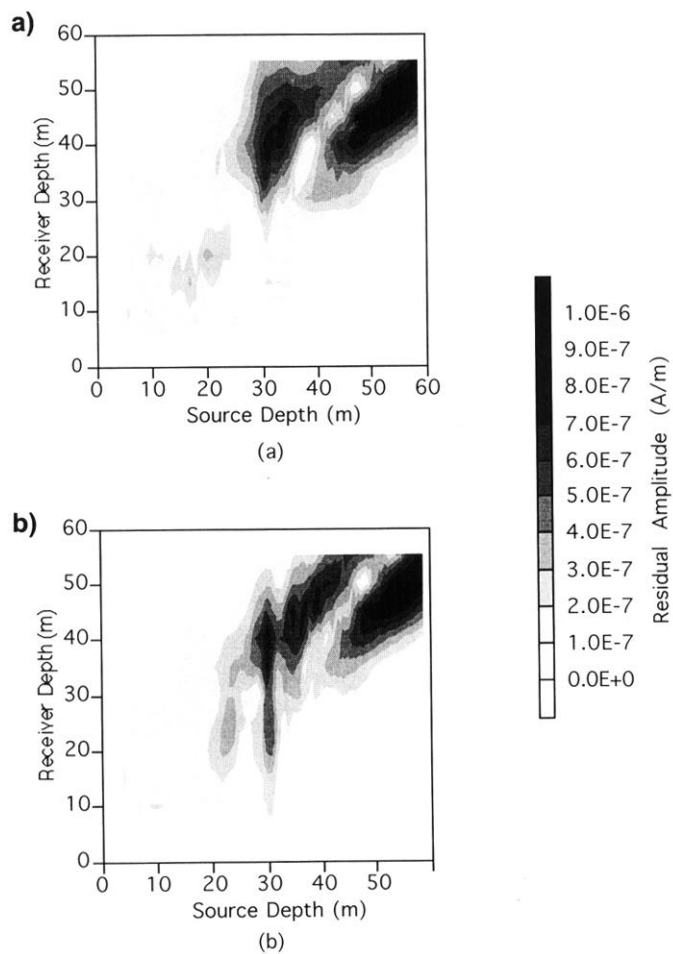


FIG. 20. Plot of the data/model misfit residual errors for the Richmond NW inversion.



Finally, because of numerical considerations, the scattered fields could not be calculated for sources within or in close proximity to the sheet.

Using the tomography results as a guide, we applied program SHEET using iterative forward modeling until the simulated difference images matched the observed difference images shown above. Results were calculated at 18.5 kHz for 23 source and 23 receiver stations separated at 2.5 m intervals from 5 m to 60 m in depth. The best fit was achieved with a 12-m by 8-m flat sheet at a depth of 31.25 m (see Figure 14). The sheet is centered about INJ1 in the east-west direction with the southern edge positioned 1 m to the south

of the injection well such that the majority of the plume lies to the north.

The images of the difference in conductivity between the half-space with and without the sheet are given in Figure 21. Notice that these results match those in Figure 19, which verifies the general migration path of the plume. Notice, however, that the simulation images exhibit arms which extend upward and downward from the injection zone. Alumbaugh (1993) has demonstrated that these differences are a result of the limitations of the model as discussed above.

Although the tomograms of the Richmond data contain 3-D artifacts, they offer images that are roughly representative of the electrical structure. In addition, the differences of the pre- and post-injection images correctly identify the direction of greatest fluid migration; this would be extremely useful in mapping water or steam floods. These results can also serve as a starting model for a more rigorous 3-D inversion such as that employed by Newman (1992). Production of these tomograms may thus be considered as the second step in a three-step process to interpret the subsurface conductivity structure.

## DISCUSSION AND CONCLUSIONS

The examples displayed above show that subsurface conductivity imaging is possible with crosswell EM induction. Although there are a number of petroleum and environmental applications that can currently benefit from this technique, the method is still in its infancy and we can expect higher data quality and higher resolution imaging in the future.

In the near term we can expect significant advances in both hardware and software. Single-frequency downhole oscillators are presently under development and a multifrequency transmitter is not too far behind. Several groups are working on borehole transient systems, although these are by nature more difficult to engineer. Imaging software is under development at several other research labs (i.e., Sandia National Laboratory, Schlumberger-Doll Research); many of these newer codes are designed to handle the high contrast anomalies and make use of multifrequency or transient data.

## ACKNOWLEDGMENTS

Partial funding for this research was provided by a consortium of energy and service companies including the research divisions of Arco, Amoco, British Petroleum, Exxon, Shell, Unocal, and Mobil Petroleum Companies, Schlumberger-Doll Research, Zonge Engineering, Noranda Technology, and Nitetsu Mining Corporation. Partial funding was also provided by the U.S. Department of Energy through Fossil Energy research under Contract W-7405-Eng-48, and the Office of Basic Energy Sciences under Contract DE-AC03-76SF0098.

We would like to thank field technicians Don Lippert, Ray Solbau from LBL's Geophysical Measurement Facility, and Louis Preciado on behalf of British Petroleum for their contributions to the data collection at Devine, and Ocean Tseng and Jim Dougherty for their contributions at Richmond field station. Chip Mansure from Sandia National Lab

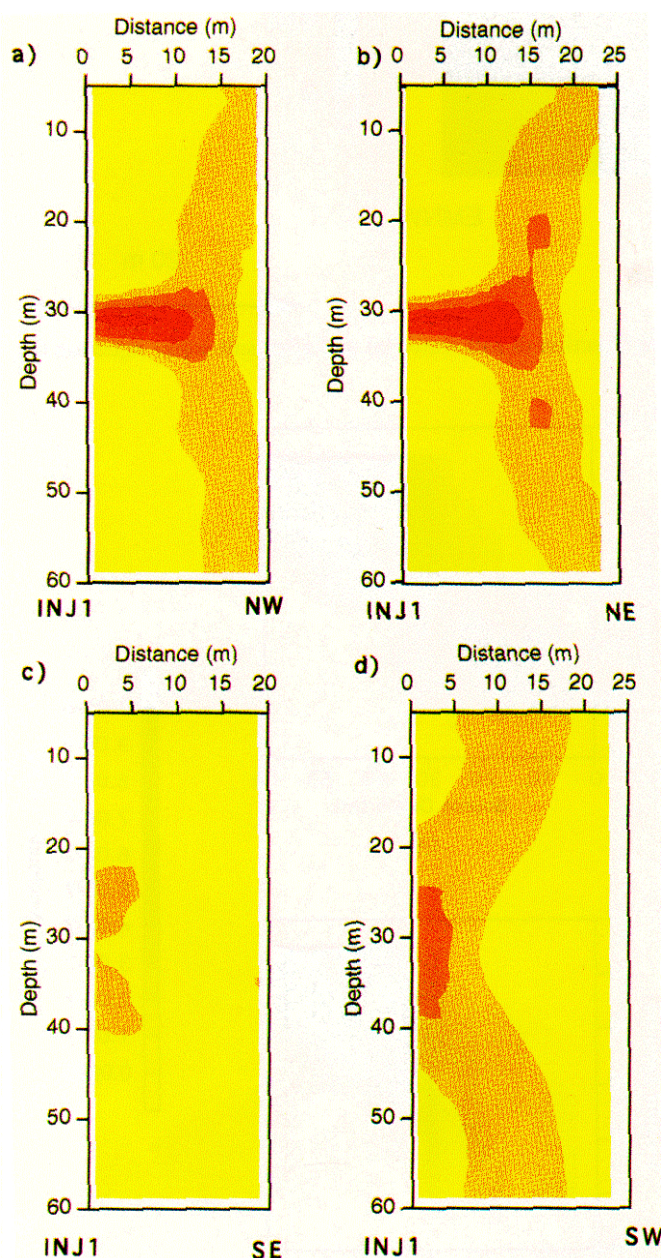


FIG. 21. Simulated difference image of the Richmond field station experiment using program SHEET. The depth of the 1s sheet is 31.25 m; its surface location is given in Figure 13.

showed us how to do "dirty" sand conductivity calculations.

## REFERENCES

- Alumbaugh, D. L., 1993, Iterative electromagnetic Born inversion applied to earth conductivity imaging., Ph.D. thesis, Univ. of California, Berkeley.
- Alumbaugh, D. L., and Morrison, H. F., 1995, Crosswell electromagnetic tomography. Theoretical and practical considerations for cylindrical geometry. *Geophysics*, 60, 846-870.
- Anderson, W. L., 1982, Adaptive nonlinear least-squares solution for constrained or unconstrained minimization problems (Subprogram NLSOL): U.S. Department of Interior Geological Survey, Open-File Report, 82-68.
- Asch, T. H., and Morrison, H. F., 1989, Mapping and monitoring electrical resistivity with surface and subsurface electrode arrays: *Geophysics*, 54, 235-244.
- Bartel, L. C., and Ranganayaki, R. P., 1990, Acquisition of controlled-source audiofrequency magnetotelluric (CSAMT) data at an active steam drive site: 59th Ann. Internat. Mtg., Soc. Expl. Geophys., Expanded Abstracts, 213-218.
- Bartel, L. C., and Wayland, J. R., 1981, Results from using CSAMT geophysical technique to map oil recovery processes: Soc. Petrol. Eng., Paper SPE 11192.
- Bevc, D., and Morrison, H. F., 1991, Borehole-to-surface electrical resistivity monitoring of a salt water injection experiment: *Geophysics*, 56, 769-777.
- Daily, W. D., and Owen, E., 1991, Cross-borehole resistivity tomography: *Geophysics*, 56, 1228-1235.
- Greaves, R. J., Beydoun, W. B., and Spies, B. R., 1991, New dimensions in geophysics for reservoir monitoring: SPE Formation Evaluation, Paper SPE 20170, 141-150.
- Harben, P., and Pihlman, M., 1988, Thermal front tracking with cross-borehole electromagnetic imaging: Proceedings from Supporting Technology for Enhanced Oil Recovery: EOR Thermal Processes. Department of Energy report DOE/BC-89/1 SP.
- Kretzschmar, J. L., Kibbe, K. L., and Witterholt, E. J., 1982, Tomographic reconstruction techniques for reservoir monitoring, Presented at the 57th Annual Fall Conference and Exhibition of the SPE and AIME, Paper SPE 10990.
- Jackson, J. D., 1962, Classical electrodynamics, John Wiley and Sons.
- Laine, E. F., 1987, Remote monitoring of the steam-flood enhanced oil recovery process: *Geophysics*, 52, 1457-1465.
- Lake, L. W., 1990, What engineers need for numerical simulation, Univ. of Ariz. and Soc. Expl. Geophys. International Symposium on Borehole Geophysics: Petroleum, Hydrogeology, Mining and Engineering Applications, Feb. 1990.
- Newman, G. A., 1992, Three-dimensional electromagnetic inversion of insufficient and inadequate data: 62nd Ann. Internat. Mtg., Soc. Expl. Geophys., Expanded Abstracts, 453-456.
- Pouch, G. W., 1987, Hydrogeological site assessment of the Engineering Geosciences Well Field at the Richmond Field Station, Contra Costa County, California: M-Sc. thesis, Univ. of California, Berkeley.
- Savit, C., 1987, New ways to study the earth, in Research needs for hydrocarbon fuels, Workshop Report on not yet visible or recoverable hydrocarbons. Houston Area Res. Ctr., U.S. Department of Energy, Office of Basic Energy Sciences, CONF-8705179m, 16-18.
- Shelton, J. L., and Cross, T. A., 1989, The influence of stratigraphy in reservoir simulation, in Cross, T. A., Ed., Quantitative dynamic stratigraphy, Prentice Hall, 589-600.
- Sherriff, R. E., 1992, Basic petrophysics and geophysics, in Sherriff, R. E., Ed., Reservoir geophysics: Soc. Expl. Geophys., 37-50.
- Shima, H., 1990, 2-D and 3-D resistivity image reconstruction by combined use of alpha centers and finite elements: 60th Ann. Internat. Mtg., Soc. Expl. Geophys., Expanded Abstracts, 554-557.
- Spies, B. R., 1992, Survey design for cross-well electromagnetics: 62nd Ann Internat. Mtg., Soc. Expl. Geophys., Expanded Abstracts, 498-501.
- Spies, B. R., and Habashy, T., 1992, Sensitivity analysis of cross-well electromagnetics. 62nd. Internat. Mtg., Soc. Expl. Geophys., Expanded Abstracts, 502-505.
- Waxman, M. H., and Thomas, E. C., 1974, Electrical conductivities in shaly sands-I. The relation between hydrocarbon saturation and resistivity index-II. The temperature coefficient of electrical conductivity: *J. of Petr. Tech.*, 213-225, Transactions AIME, 257.
- Wayland, J. R., Lee, D. O., and Cabe, T. J., 1984, Mapping of a steamflood in a Utah tar sand by controlled source magnetotelluric survey: SPE/DOE 12675, SPE/DOE 4th Symp. on Enhanced Oil Recovery.
- Weidelt, P., 1981, Dipole Induction on a thin plate with host medium and overburden. Res project NTS 83 no 3. 89727, Federal Inst Earth Sciences and raw materials, Hannover, West Germany.
- Zhou, Q., 1989, Audio frequency numerical modeling and tomographic inversion for reservoir evaluation: Ph.D. thesis, Univ. of California, Berkeley.